

See discussions, stats, and author profiles for this publication at: <https://www.researchgate.net/publication/24377496>

# Direct Detection and Characterization of Chloride in the Active Site of the Low-pH Form of Sulfite Oxidase Using Electron Spin Echo Envelope Modulation Spectroscopy, Isotopic Label...

ARTICLE *in* INORGANIC CHEMISTRY · MAY 2009

Impact Factor: 4.76 · DOI: 10.1021/ic801787s · Source: PubMed

---

CITATIONS

25

---

READS

131

7 AUTHORS, INCLUDING:



[Dmitry Ganyushin](#)

27 PUBLICATIONS 706 CITATIONS

SEE PROFILE



[Christoph Riplinger](#)

Princeton University

19 PUBLICATIONS 362 CITATIONS

SEE PROFILE



[Kayunta johnson-winters](#)

University of Texas at Arlington

19 PUBLICATIONS 370 CITATIONS

SEE PROFILE

Published in final edited form as:

*Inorg Chem.* 2009 June 1; 48(11): 4743–4752. doi:10.1021/ic801787s.

# Direct Detection and Characterization of Chloride in the Active Site of the Low-pH Form of Sulfite Oxidase Using ESEEM Spectroscopy, Isotopic Labeling, and DFT Calculations

Eric L. Klein<sup>†</sup>, Andrei V. Astashkin<sup>†</sup>, Dmitry Ganyushin<sup>‡</sup>, Christoph Riplinger<sup>‡</sup>, Kayunta Johnson-Winters<sup>†</sup>, Frank Neese<sup>\*,‡</sup>, and John H. Enemark<sup>\*,†</sup>

Department of Chemistry and Biochemistry, University of Arizona, 1306 E. University Blvd., Tucson, Arizona 85721, Institut für Physikalische und Theoretische Chemie, Universität Bonn, Wegelerstrasse 12, 53115 Bonn, Germany

Eric L. Klein: ; Andrei V. Astashkin: ; Dmitry Ganyushin: ; Christoph Riplinger: ; Kayunta Johnson-Winters: ; Frank Neese: ; John H. Enemark: jenemark@u.arizona.edu

## Abstract

Electron spin echo envelope modulation (ESEEM) investigations were carried out on samples of the low-pH (*lpH*) form of vertebrate sulfite oxidase (SO) prepared with <sup>35</sup>Cl- and <sup>37</sup>Cl-enriched buffers as well as with buffer containing the natural abundance of Cl isotopes. The isotope-related changes observed in the ESEEM spectra provide direct and unequivocal evidence that Cl<sup>−</sup> is located in close proximity to the Mo(V) center of *lpH* SO. The measured isotropic hyperfine interaction constant of about 4 MHz (<sup>35</sup>Cl) suggests that the Cl<sup>−</sup> ion is either weakly coordinated to Mo(V) at its otherwise vacant axial position, *trans* to the oxo ligand, or is hydrogen-bonded to the equatorial exchangeable OH ligand. Scalar relativistic all-electron density functional theory (DFT) calculations of the hyperfine and nuclear quadrupole interaction parameters, along with steric and energetic arguments, strongly support the possibility that Cl<sup>−</sup> is hydrogen-bonded to the equatorial OH ligand rather than being directly coordinated to the Mo(V).

## INTRODUCTION

Sulfite oxidase (SO) is an essential molybdoenzyme that catalyzes the two-electron oxidation of sulfite (SO<sub>3</sub><sup>2−</sup>) to sulfate (SO<sub>4</sub><sup>2−</sup>). The fully oxidized SO catalytic center features a Mo(VI) ion that is coordinated by two oxo ligands and three sulfur donor atoms in a roughly square pyramidal geometry.<sup>1, 2</sup> One of the oxo ligands occupies the axial apex, pointing into the protein, while the other oxo ligand occupies one of the four equatorial positions and is oriented directly into a positively charged channel that leads away from the catalytic site toward the protein surface. The three sulfur donor atoms, one from Cys and the remaining two from the dithiolene unit of molybdopterin (MPT), a cofactor that is unique to Mo/W enzymes, occupy the remaining positions of the equatorial plane.

During catalysis, SO<sub>3</sub><sup>2−</sup> enters the active site and reacts with the equatorial oxo ligand, reducing the Mo(VI) to Mo(IV) and forming a SO<sub>4</sub><sup>2−</sup>-bound Mo(IV) species.<sup>3</sup> SO<sub>4</sub><sup>2−</sup> is then hydrolyzed

\*To whom correspondence should be addressed. E-mail: neese@thch.uni-bonn.de (F.N.), jenemark@u.arizona.edu (J.H.E.).

<sup>†</sup>University of Arizona

<sup>‡</sup>Universität Bonn

## SUPPORTING INFORMATION

Atom coordinates (XYZ) for all of the computational models; this material is available free of charge via the Internet at <http://pubs.acs.org>.

from Mo, and the active center is oxidized stepwise back to its Mo(VI) resting state via a paramagnetic Mo(V)-OH intermediate.

The Mo(V)-OH intermediate has been the focus of many electron paramagnetic resonance (EPR) studies that have yielded important details about the structure of the enzyme active site as a function of solution pH, anions present in the media, the method of generation of the Mo(V) state, and specific enzyme point mutations. Early continuous wave (CW) EPR investigations established that the Mo(V) center of SO exhibits different signals depending on pH and presence of inhibiting anions (e.g.  $\text{PO}_4^{3-}$  and  $\text{AsO}_3^{3-}$ ).<sup>4–6</sup> For example, the Mo(V) centers from chicken SO (cSO) prepared at  $\text{pH} \leq 7.5$  and  $\text{pH} \geq 9$  have differing sets of principal  $g$ -values, and the low-pH EPR signal clearly displays hyperfine splittings from the nearby exchangeable proton of the hydroxo ligand.<sup>6</sup> Structurally distinct forms of SO corresponding to these signals are generally referred to as the low-pH (*lpH*) or high-pH (*hpH*) forms. Similar *lpH* and *hpH* forms have also been identified for wild-type (*wt*) and mutant SO from human (hSO),<sup>7</sup> plant (*Arabidopsis thaliana*, At-SO),<sup>8</sup> and the bacterial sulfite-oxidizing enzyme (SOE), sulfite dehydrogenase (SDH).<sup>9</sup> Recent pulsed EPR measurements have also detected a *blocked* form of SOEs, which retains sulfate as a ligand in the Mo(V) state.<sup>10–12</sup>

Based on the effects of buffer pH and  $\text{Cl}^-$  concentration on the CW EPR spectra of cSO, Bray *et al.* proposed that  $\text{Cl}^-$  should be an integral component of the Mo(V) center in the *lpH* form of SO.<sup>4</sup> This possibility was later supported, albeit inconclusively, by extended X-ray absorption fine structure (EXAFS) experiments.<sup>13</sup> Recently, this system was revisited by Doonan *et al.*, who also employed CW EPR, but with the *lpH* SO samples prepared using isotopically pure  $^{35}\text{Cl}^-$  or  $^{37}\text{Cl}^-$  (both  $I=3/2$ ).<sup>14</sup> While some differences between the CW EPR spectra of the pure isotopic Cl preparations were arguably observable, the extremely subtle scale of those differences makes their unequivocal interpretation impossible. Thus, unfortunately, neither CW EPR nor EXAFS can be effectively used to definitively identify  $\text{Cl}^-$  in this system or properly characterize its interaction with the enzyme. The spectral resolution of CW EPR in frozen samples is very low, and EXAFS cannot distinguish between Cl and S nuclei. However, CW EPR spectra of *lpH* SO samples prepared with  $\text{Br}^-$  (natural abundance = 50.69%  $^{79}\text{Br}$  and 49.31%  $^{81}\text{Br}$ ; both  $I=3/2$ ) and  $^{127}\text{I}^-$  ( $I=5/2$ ) showed resolvable  $\text{Br}^-$  and  $\text{I}^-$  *hfi* that were  $\sim 4.5$  greater than the *hfi* from Cl, supporting the possibility of halide coordination to the Mo(V) center.<sup>14</sup>

Beyond CW EPR and EXAFS, the possibility of  $\text{Cl}^-$  coordination has been used to explain some of the recurrent features in the electron spin echo envelope modulation (ESEEM) spectra of SO,<sup>15, 16</sup> and another molybdoenzyme, dimethylsulfoxide reductase (DMSOR),<sup>17</sup> but this possibility was never resolved. In this work, we report the ESEEM results for *lpH* SO samples prepared with natural abundance  $\text{Cl}^-$  (Cl-SO) and with isotopically pure  $^{35}\text{Cl}^-$  ( $^{35}\text{Cl}$ -SO) and  $^{37}\text{Cl}^-$  ( $^{37}\text{Cl}$ -SO). These results unequivocally and directly confirm the presence of  $\text{Cl}^-$  in close proximity to the Mo(V) center of the *lpH* form of SO and provide the first reliable hyperfine (*hfi*) and nuclear quadrupole (*nqi*) interaction parameters for the chlorine nucleus. The structural implications of the parameters obtained are discussed using density functional theoretical (DFT) calculations, spectroscopic data from model oxomolybdenum compounds,<sup>18</sup> and the available general structural information related to the molybdenum center and its protein environment.

## MATERIALS AND METHODS

### Sample preparation

Reagent grade natural abundance NaCl (75.78%  $\text{Na}^{35}\text{Cl}$  and 24.22%  $\text{Na}^{37}\text{Cl}$ ) was obtained from VWR Scientific Products,  $\text{Na}^{35}\text{Cl}$  (>99 atom %) was obtained from Sigma-Aldrich Chemical Co, and  $\text{Na}^{37}\text{Cl}$  (>94 atom %) was obtained from Cambridge Isotope Laboratories,

Inc. Separate highly purified Cl-SO,  $^{35}\text{Cl}$ -SO, and  $^{37}\text{Cl}$ -SO samples were, with the exception of the Cl isotope identity, each identically prepared according to a published procedure.<sup>19</sup> Frozen samples for ESEEM were prepared using 2 mg of *wt* cSO in 60  $\mu\text{L}$  of buffer (pH=6) containing 50 mM bis-tris-propane and 100 mM NaCl (natural abundance,  $^{35}\text{Cl}$ , or  $^{37}\text{Cl}$ ).<sup>4</sup> Immediately prior to freezing in liquid nitrogen, the enzyme was reduced using a 20-fold excess of sodium sulfite. For the sample that was prepared without added NaCl, *wt* hSO instead of *wt* cSO (due to availability) was used, and the entire preparation was otherwise identical.

### ESEEM measurements

ESEEM experiments were performed on home-built  $K_a$ -band (26 – 40 GHz)<sup>20, 21</sup> and X/ $K_u$ -band (8 – 18 GHz)<sup>21</sup> pulsed EPR spectrometers at microwave (mw) frequencies,  $\nu_{\text{mw}}$ , of about 29 GHz and 17 GHz, respectively. The measurement temperature in each experiment was 21 K. Numerical simulations of the ESEEM spectra were performed using the SimBud software, available free-of-charge from the University of Arizona website.<sup>21</sup>

### Theoretical calculations

$^{35}\text{Cl}$  and  $^{17}\text{O}$  *hfi* and *nqi* parameters were calculated using the ORCA computational package.<sup>22</sup> Geometry optimizations were performed using the BP86 functional<sup>23</sup> in conjunction with the all-electron TZVP basis<sup>24</sup> in its scalar relativistic re-contraction reported in ref <sup>25</sup> and modeling the protein environment through dielectric continuum methods (conductor like screening model, COSMO),<sup>26</sup> using a dielectric constant of four.<sup>27</sup> Density fitting<sup>28</sup> was used to accelerate these calculations. Relativistic effects were treated at the level of the zeroth order regular approximation (ZORA)<sup>29</sup> in one-component form using the model potential of van Wüllen<sup>30</sup> (as implemented in ORCA). For geometry optimizations, the one-center ZORA scalar relativistic correction was employed.<sup>31</sup>

Starting coordinates for different structural models describing the interaction of  $\text{Cl}^-$  with the active center were based on the X-ray crystal structures of *wt* cSO.<sup>2, 32</sup> The cSO active site structures were modified to include the equatorial hydroxo ligand (replacing the equatorial oxo ligand from the crystal structure) and the  $\text{Cl}^-$  (except for model E2, where the  $\text{Cl}^-$  coordinates in the protein were available). Following literature precedent,<sup>14, 33</sup> in the calculations for models A1 and A2, with axially coordinated  $\text{Cl}^-$  (Figures 7 and 9, respectively, see below), the pterin portion of the molybdopterin cofactor was omitted. This simplification was also used for model E1 (Figure 10). In addition, the cysteinate residue was replaced by ethanethiolate for the simplified axial model A1 (Figure 7), and the ethanethiolate dihedral angles were constrained to their crystal structure values relative to the axial  $\text{Mo(V)}\equiv\text{O}$  bond in order to prevent unrealistic rotation of that group during geometry optimization. Principal *g*-values and the  $^{35}\text{Cl}$  and  $^{17}\text{O}$  *hfi* and *nqi* parameters were calculated using the B3LYP functional,<sup>34</sup> the TZVP basis set, the ZORA method, and COSMO (using a dielectric constant of four). Since the scalar relativistic TZVP basis set is less heavily contracted than its nonrelativistic counterpart, further decontraction is not necessary in order to obtain accurate *hfi* and *nqi* predictions close to the basis set limit. Since we have previously found that the inclusion of picture change effects in the ZORA-4 formalism<sup>35</sup> did not improve the quality of calculated quadrupole couplings,<sup>36</sup> we did not apply such corrections here. For the correct ZORA calculation of hyperfine couplings,<sup>37</sup> it is nevertheless necessary to apply the relativistic formalism.

## RESULTS AND DISCUSSION

### 1. Chloride in *lpH wt SO*

The EPR spectra of *lpH* Cl-SO,  $^{35}\text{Cl}$ -SO, and  $^{37}\text{Cl}$ -SO were identical to those reported previously for *lpH* SO.<sup>4, 14</sup> Since no Cl-related splittings are directly observable in any of these

spectra, we performed ESEEM experiments at several EPR positions, including the low-, intermediate-, and high-field EPR turning points ( $g_z$ ,  $g_y$ , and  $g_x$ , respectively). From these measurements it became immediately clear that the low-frequency ESEEM of *lpH* SO depends on the specific Cl isotope composition of the buffers. As an example, the hyperfine sublevel correlation (HYSCORE)<sup>38</sup> spectra of *lpH* Cl-SO, <sup>35</sup>Cl-SO, and <sup>37</sup>Cl-SO obtained at  $g_y$  are shown in Figures 1a through 1c, respectively. Only the (++) quadrant of each spectrum is shown because no features exceeding the noise level were observed in the (-+) quadrants. While the HYSCORE spectra differ from each other, all of the cross-peaks that are observed in Figure 1a (corresponding to Cl-SO) are found in either Figure 1b or in Figure 1c (corresponding to <sup>35</sup>Cl-SO and <sup>37</sup>Cl-SO, respectively). These results provide direct evidence that the low-frequency ESEEM in *lpH* SO originates from a Cl nucleus.

The observation of the Cl ESEEM requires that the Cl nucleus be in close proximity to Mo(V). In order to obtain more specific structural information, it is necessary to estimate the Cl *hfi* and *nqi* parameters from the ESEEM spectra. To this end, we will mostly consider the data for the sample of <sup>35</sup>Cl-SO.

The HYSCORE spectra of *lpH* <sup>35</sup>Cl-SO obtained at  $g_z$ ,  $g_y$ , and  $g_x$  are presented in Figure 2. Each individual spectrum represents a sum of spectra obtained at several different time intervals between the first two mw pulses,  $\tau$ . This is a common practice for reducing loss of information due to  $\tau$ -dependent spectral blind spots. In each spectrum, the cross-peaks are centered about the Zeeman frequency of <sup>35</sup>Cl ( $\nu_1 \sim 4.5$  MHz at the magnetic fields  $B_0 \sim 1060 - 1080$  mT used in these experiments). According to theoretical analysis of the situations of strong and weak *nqi* for nuclei with half-integer spin,<sup>10, 39, 40</sup> this indicates that the *nqi* of the Cl nucleus observed in the ESEEM spectra is rather weak:  $e^2Qq/h \leq \nu_1 \pm A/2$ , where  $e^2Qq/h$  is the quadrupole coupling constant and  $A$  is the *hfi* constant ( $A \approx a_{\text{iso}} + T_{\text{zz}}$ , where  $a_{\text{iso}}$  is the isotropic *hfi* constant and  $T_{\text{zz}}$  is the secular component of the anisotropic *hfi* tensor). In this case, the splitting between the cross-peaks gives a good estimate of the *hfi*. One can see that the *hfi* is only weakly anisotropic, and the mean splitting between the cross-peaks gives an estimate of the average isotropic *hfi* constant,  $\langle a_{\text{iso}} \rangle \sim 3 - 4$  MHz. The spectroscopic situation is, therefore, that of weak *hfi* ( $\nu_1 > |A/2|$ ).

In the case of weak *nqi*, ESEEM spectra of a nucleus with any spin are expected to be qualitatively similar to those of a nucleus with spin  $I = 1/2$ .<sup>39, 40</sup> Indeed, the cosine Fourier transform (FT) spectrum of two-pulse ESEEM (Figure 3) shows the fundamental lines at the frequencies  $\nu_{\alpha,\beta} \approx |\nu_1 \pm A/2|$  and combination lines at the frequencies  $\nu_{\sigma} = \nu_{\alpha} + \nu_{\beta} \approx 2\nu_1$  and  $\nu_{\delta} = |\nu_{\alpha} - \nu_{\beta}| \approx |A|$ . The fundamental lines have a positive amplitude and are contributed to by all of the  $\Delta m_1 = 1$  nuclear transitions, but dominated by  $| -1/2 \rangle \leftrightarrow | +1/2 \rangle$  transitions which are broadened by *nqi* to second order. The sum ( $\nu_{\sigma}$ ) and difference ( $\nu_{\delta}$ ) combination lines have negative amplitudes and are predominantly broadened by the *nqi* and *hfi*, respectively.

The fact that the sum combination line is not broadened by the *hfi* (to first order), but rather, is broadened or split into a multiplet by the *nqi*, makes this line useful for estimating the quadrupole coupling constant.<sup>40</sup> However, two-pulse ESEEM is not the best technique for this purpose because its relatively short ESE signal decay (determined by the transverse relaxation time,  $T_2$ ) results in significant additional broadening of the spectral lines. In contrast, the stimulated ESE signal decay is determined by the longitudinal relaxation time,  $T_1 \gg T_2$ . Consequently, the broadening caused by the relaxation decay is usually negligible in spectra of stimulated ESEEM and spectra of other techniques that are based on monitoring the stimulated ESE signal. One such technique, integrated (over the time interval between the first and second mw pulses,  $\tau$ ) four-pulse ESEEM spectroscopy,<sup>41, 42</sup> has been previously used in our laboratory to determine the weak *nqi* of the oxo-<sup>17</sup>O ligand in the Mo(V) center of SO and in a model oxo-molybdenum complex.<sup>40</sup>

Trace 1 in Figure 4 shows the field-integrated<sup>10, 18</sup> (FI) spectrum of the  $\tau$ -integrated four-pulse ESEEM obtained for the  $lpH$   $^{35}\text{Cl}$ -SO. This spectrum has the same structure as the two-pulse ESEEM spectrum shown in Figure 3, apart from the difference combination line ( $\nu_\delta$ ) which is considerably suppressed in the integrated four-pulse spectra under the weak  $hfi$  conditions.<sup>42</sup> The sum combination line in this spectrum is broadened by the  $nqi$  to a width of about 2 MHz. For comparison, trace 2 shows the four-pulse ESEEM spectrum for  $lpH$   $^{37}\text{Cl}$ -SO. These spectra are clearly similar, with the spectrum of  $^{37}\text{Cl}$ -SO being compressed along the frequency axis with respect to that of  $^{35}\text{Cl}$ -SO by about 20%, in agreement with the ratio of magnetic ( $\mu(^{35}\text{Cl})/\mu(^{37}\text{Cl}) \approx 1.2$ ) and quadrupole ( $Q(^{35}\text{Cl})/Q(^{37}\text{Cl}) \approx 1.27$ ) moments of the Cl isotopes.

In order to obtain quantitative information about the anisotropic  $hfi$  and  $nqi$  parameters, numerical simulations of the ESEEM spectra were performed. While it is possible, in principle, to estimate the anisotropic  $hfi$  constant from the width of the HYSCORE cross-peaks, this width can be significantly influenced by the static distribution of the  $a_{iso}$  values and by the  $nqi$ . A more reliable measure of the anisotropic  $hfi$  is the amplitude of the two-pulse ESEEM. To simplify the simulations, an approach similar to that of our previous work, where the FI ESEEM spectra are simulated,<sup>10, 18</sup> was employed here.

As a result of the simulations, the anisotropic  $hfi$  constant of  $^{35}\text{Cl}$  was estimated as  $|T_\perp| = 0.2 \pm 0.05$  MHz, with  $a_{iso}$  being within the range of 4 – 5 MHz, slightly greater than the qualitative estimate from the HYSCORE spectra. The relative sign of  $T_\perp$  (with respect to  $a_{iso}$ ) could not be reliably determined, although the negative values (assuming  $a_{iso} > 0$ ) resulted in somewhat better fits. As an example, the dashed line in Figure 3 shows the simulated spectrum of a  $^{35}\text{Cl}$  nucleus with  $a_{iso} = 4$  MHz,  $T_\perp = -0.2$  MHz,  $e^2Qq/h = 3$  MHz,  $\eta = 0.5$ , and the angle between the main axes of  $hfi$  and  $nqi$  of  $90^\circ$ . These  $nqi$  parameters gave a reasonable fit to the four-pulse ESEEM spectra (Figure 4, dashed lines).

We have to note that, while the quality of the simulations is acceptable for practical purposes, the simulated spectra do not reproduce the experimental data perfectly. For example, the  $\nu_\delta$  line in the simulated two-pulse spectrum of Figure 3 is shifted to lower frequencies by about 0.7 MHz (from 4.5 to 3.8 MHz) and has a larger amplitude, the fundamental lines in the simulated integrated four-pulse spectra have noticeably smaller amplitudes than the experimental lines in the regions close to  $\nu_1$ , and the broad line at 13 MHz is present in the simulated four-pulse spectrum, but not in the experimental one. All of these features can be attributed to the presence of a static distribution of  $hfi$  and  $nqi$  parameters related to small structural inhomogeneities that are always present in frozen solutions.

The 13 MHz feature of Figure 3, for example, represents the  $\Delta m_I = 2$  line located at the frequency  $\nu_{\Delta m=2} \approx 2\nu_1 + A$ . For spin  $I = 3/2$ , this is actually a doublet corresponding to the frequencies of  $|-3/2\rangle \leftrightarrow |1/2\rangle$  and  $|-1/2\rangle \leftrightarrow |3/2\rangle$  nuclear transitions split by the weak  $nqi$ . The statistical distribution of both  $A$  and the  $nqi$  will broaden this line and reduce its amplitude. The difference combination frequency is approximately equal to the  $hfi$  constant;  $\nu_\delta \approx A$ . The distribution in  $A$  will reduce the amplitude of this line in the simulated spectrum and improve its agreement with the experiment. The down-frequency shift can be corrected by introducing the asymmetric distribution with a sharp cutoff at  $A \sim 4.5$  MHz. The amplitude of the fundamental lines at the frequencies close to  $\nu_1$  can be improved by introducing the distribution in  $A$  or  $nqi$ , correlated with the increase in the anisotropic  $hfi$  for smaller splittings.

While the qualitative explanation above shows that the discrepancies between the simulated and experimental spectra could technically be eliminated by introducing the distributed  $hfi$  and  $nqi$  parameters, such simulations are not realistic at present primarily because of the sheer number of unknown parameters involved. Even for simulations of FI spectra with fixed parameters, there are already eight unknown variables (three  $hfi$  parameters, two  $nqi$



parameters, and three Euler angles describing the relative orientation of the *hfi* and *nqi* tensors). For simulations with distributed parameters, more variables describing the distributions and their correlations must be introduced. While obtaining a better fit under such circumstances is theoretically possible, such efforts would also be extremely time consuming and would not contribute to the significance of the results. In spite of the imperfect agreement between the experimental spectra and the spectra simulated with fixed parameters, however, the fact that the *hfi* and *nqi* distributions for  $^{35}\text{Cl}$  in SO are rather narrow (as can be seen from the extent of correlation ridges in HYSCORE spectra of Figure 2) ensures that the parameters obtained represent a good approximation of the mean values of the distributed parameters.

In the numerical simulations, we have assumed that each Mo(V) center of *lpH* SO is interacting with a single  $\text{Cl}^-$  in its vicinity. Assuming more than one nearby  $\text{Cl}^-$  would result in smaller estimates for  $T_{\perp}$ , while assuming less than one  $\text{Cl}^-$  (that is, that some of the Mo(V) centers contributing to the *lpH* SO EPR signal do not have a nearby  $\text{Cl}^-$ ) would result in larger  $T_{\perp}$  values. The spectroscopic complexity does not allow this problem to be resolved using ESEEM simulations, and other factors must be taken into account. The possibility of multiple chlorides near the Mo(V) center will be addressed in the context of the active site structure and the results of the DFT calculations (below). The heterogeneous situation, with less than one neighboring  $\text{Cl}^-$  ion per Mo(V) center, is not likely for two reasons. First, the structural rearrangements around the Mo(V) center caused by presence or absence of  $\text{Cl}^-$  will probably result in measurable changes of the principal *g*-values, which is not observed. Second, for all studied samples of *lpH* SO (see the following section) the Cl ESEEM amplitudes are similar, while for a heterogeneous system at least some variation would be expected.

As an example, for hSO at pH = 6.5, prepared without adding  $\text{Cl}^-$  to the buffer, the *lpH* EPR signal was observed, and the Cl ESEEM amplitude was similar to that of *lpH* SO prepared with buffer containing 100 mM  $\text{Cl}^-$ . Figure 5 shows the HYSCORE spectrum of the sample prepared with “ $\text{Cl}^-$ -free” buffer, where the only known source of  $\text{Cl}^-$  is from trace contamination ( $[\text{Cl}^-] \sim 1 \text{ mM}$ ).<sup>43</sup> Notably, the contaminant  $[\text{Cl}^-]$  is comparable to the estimated enzyme concentration itself ( $\sim 300 \mu\text{M}$ ), supporting the argument that  $\text{Cl}^-$  binding to the active center is homogeneous, with each of the Mo(V) centers having a  $\text{Cl}^-$  in its vicinity.

## 2. Chloride in other types of SO

While the analysis of the  $K_a$ -band Cl ESEEM spectra proved to be relatively simple, the ESEEM amplitudes were rather small. The *hfi* parameters suggest that the ESEEM amplitude should increase if the experiments are performed at  $K_u$  band since, in that case, the cancellation condition for the Zeeman and hyperfine interactions can be reached (for  $^{35}\text{Cl}$  with  $a_{\text{iso}} \sim 4 \text{ MHz}$  the optimal mw frequency would be about 14.9 GHz). Therefore, as a qualitative test for the presence of  $\text{Cl}^-$ , we performed a series of  $K_u$ -band experiments on samples of SOEs from different *wt* and mutant organisms (prepared at different pH values). In these experiments, the Cl ESEEM was only observed for the *lpH* form of the enzymes, regardless of the sample type. Specifically, it was observed in *lpH wt* hSO, *wt* cSO, Y343F hSO (the *lpH*-type signal observed at pH  $\sim 9.0$ <sup>12</sup>), and *lpH* Y236F SDH<sup>44</sup> (for *wt* SDH only the *lpH*-type signal is observed at all pH values<sup>9</sup>). Additionally, the Cl ESEEM amplitude was similar in all cases, supporting the argument of the previous section that the Mo(V) center of *lpH* SOEs have a single nearby  $\text{Cl}^-$ . The *hpH*-type signal did not reveal any Cl ESEEM, and the same was true for the *blocked* ( $\text{SO}_4^{2-}$ -bound) form of SO observed for At-SO,<sup>10</sup> Y343F hSO,<sup>12</sup> R160Q hSO,<sup>11</sup> and R55Q SDH<sup>45</sup> at low pH. To illustrate these results, Figure 6 shows representative  $K_u$ -band primary ESEEM spectra of several samples of SOEs obtained at the  $g_Y$  EPR turning point.

### 3. Structural implications of the EPR results

The  $hfi$  of the Cl nucleus in *lpH* SO obtained in this work ( $a_{iso} \sim 4$  MHz and  $|T_{\perp}| \sim 0.2$  MHz) is significantly weaker than that in the model Mo(V) complexes with equatorially coordinated chloride ( $a_{iso} \sim 10$  MHz and  $T_{\perp} \sim -10$  MHz).<sup>18</sup> Also, the  $nqi$  estimated in this work ( $\sim 3$  MHz) is about one order of magnitude smaller than the  $nqi$  constants previously obtained for covalently bound  $Cl^{-}$ . In model complexes containing the *cis*-oxo-Mo(V)-Cl fragment,  $Cl^{-}$  has  $nqi$  constants of tens of MHz.<sup>18, 46</sup> This comparison eliminates any possibility of inner-sphere equatorial coordination of  $Cl^{-}$  to Mo(V) in *lpH* SO, in agreement with the available structural knowledge for the molybdenum center of SO discussed in the Introduction. However, the fact that the isotropic  $hfi$  constant of Cl in SO is fairly large suggests that there should be a through-bond pathway for the spin polarization of the Cl electronic orbitals. This spin polarization results in a spin population of the Cl valence orbitals of up to 2% (if pure p-type valence orbitals are assumed). Two distinct structural possibilities that may allow for such spin polarization on the  $Cl^{-}$  will be considered in order to explain the spectroscopic findings of this work.

The first considers the  $Cl^{-}$  to be directly coordinated to the Mo(V). The only available position for direct coordination is axial, *trans* to the oxo ligand. Although the possibility of  $Cl^{-}$  being weakly coordinated at this position has been previously proposed,<sup>13, 14, 18</sup> the absence of solid spectroscopic data for  $Cl^{-}$  in either the enzyme or in structurally defined mononuclear *trans*-oxo-Mo(V)-Cl systems has prevented direct spectroscopic comparisons.

The other possibility is that  $Cl^{-}$  is located in the second coordination sphere, near the equatorial plane of the Mo(V) center. The most likely structure that would provide a through-bond spin polarization pathway is H-bonding of the  $Cl^{-}$  to the equatorial OH ligand of the Mo(V) center. Several specific structural models falling into each of these two categories (direct axial coordination or second-sphere equatorial coordination) were investigated in detail by DFT calculations, as described in the following section.

### 4. Density functional theory (DFT) calculations

In order to begin assessing the first possibility, direct axial  $Cl^{-}$  coordination, we first performed a series of DFT calculations on highly simplified and constrained computational models where the  $^{35}Cl$  and  $^{17}O$   $hfi$  and  $nqi$  parameters, as well as the principal  $g$ -values of the models, were calculated as a function of the Mo(V)-Cl distance,  $R_{MoCl}$  (model A1, Figure 7). Since some flexibility in  $R_{MoCl}$  within the SO active site could possibly exist, the initial calculations were primarily designed to provide qualitative estimates of the effect of  $R_{MoCl}$  on each of these spectroscopic parameters. Secondly, the results from these models could be used to establish a preliminary range of  $R_{MoCl}$  where the calculated parameters may be in agreement with the experimental values, thus providing a foundation for more detailed computational work. While the  $^{17}O$  nuclei of the axial oxo and equatorial OH ligands are not specifically the subject of this study, we reasoned that their spectroscopic parameters would be affected by the proximity of  $Cl^{-}$  to the Mo(V) center and could provide additional restrictions to the location of the  $Cl^{-}$ .

In these preliminary calculations, the orientation of the equatorial hydroxo ligand was constrained to the equatorial plane with the OH bond turned in the direction of the cysteinate sulfur in accordance with the accepted structure of the Mo(V) intermediate in the *lpH* form.<sup>16</sup> Chloride was introduced at a range of distances from the Mo(V) center with the angle  $O\equiv Mo-Cl$  fixed at  $180^{\circ}$ . In separate calculations,  $R_{MoCl}$  was fixed and the geometry was optimized subject to the constraints described above and in the experimental section. Properties were then calculated from the optimized structures.



Figure 8 shows the general dependence of the calculated  $hfi$  and  $nqi$  parameters of  $^{35}\text{Cl}$  and the  $^{17}\text{O}$  ligands as a function of  $R_{\text{MoCl}}$  for the simplified models, represented by model A1 of Figure 7. For comparison, the shaded areas in Figure 8 represent the values of the corresponding experimental parameters. The optimal  $R_{\text{MoCl}}$  (where the  $R_{\text{MoCl}}$  was fully relaxed) in terms of the total energy was calculated to be 2.80 Å, but the energy well was very shallow with a depth of only ~1 kcal/mol. The very low Mo-Cl bond dissociation energy reflects the strong *trans* effect from the oxo ligand. It has been proposed that within the constrained environment of the enzyme, however, the active site Arg that is located very near to the proposed axial binding site (R138 in cSO, R160 in hSO, R55 in bacterial SDH) may play a significant role in stabilizing the  $\text{Cl}^-$  in that position.<sup>14, 18</sup> This possibility is addressed in greater detail (below) through DFT calculations that include the Arg residue.

Disregarding such protein interactions for the moment, however, for  $R_{\text{MoCl}}$  over the range of 2.5 – 4.0 Å, both the  $hfi$  and  $nqi$  of  $^{35}\text{Cl}$  differ significantly from the experimentally obtained values for *lpH* SO, while the calculated  $g$ -values agree reasonably well (Table 1). The difference between the calculated and experimental  $a_{\text{iso}}$  minimizes for  $R_{\text{MoCl}}$  from 2.5 to 3.5 Å, although it still remains fairly large (about 1.5 MHz calculated vs. ~4 MHz experimental). The calculated  $nqi$  reaches values up to 20 MHz, much larger than the experimental value of  $e^2Qq/h \sim 3$  MHz. Compared to  $\text{Cl}^-$ , the  $^{17}\text{O}$  parameters calculated for larger  $R_{\text{MoCl}}$  values are in better agreement with the experimental values.<sup>20, 40, 47, 48</sup> At  $R_{\text{MoCl}} < 2.8$  Å, the effect of the  $\text{Cl}^-$  on these parameters becomes more significant, and  $R_{\text{MoCl}} \sim 2.7$  Å can be loosely identified as a lower possible limit of the axial Mo-Cl distance. It is not possible to establish an upper limit for  $R_{\text{MoCl}}$  from the  $^{17}\text{O}$  parameters alone, but based on the  $^{35}\text{Cl}$   $hfi$ , it is unlikely to exceed 3.5 Å since for greater distances the isotropic  $hfi$  constant of the Cl nucleus rapidly approaches zero.<sup>49</sup>

It should be mentioned that this approach to the DFT calculations differs (beyond fundamental computational methods) from that of Doonan *et al.*<sup>14</sup> in that they incorporated a nearby Tyr residue into their calculations. Specifically, one of their conclusions was that the active site Tyr (Y343 in hSO) plays an important role in stabilizing the  $\text{Cl}^-$  coordination to Mo(V) and that without the Tyr H-bond interaction with Mo(V)-OH,  $\text{Cl}^-$  would dissociate from the complex. Our calculations on model A1 (Figure 7), however, indicate that the inclusion of Tyr (or any other residue) is not necessary to prevent  $\text{Cl}^-$  dissociation. Moreover, we have demonstrated experimentally from pulsed EPR studies that the *lpH*-type signal shows  $\text{Cl}^-$  in close proximity to Mo(V), even in the samples where the active site Tyr has been mutated to Phe (Y343F hSO,<sup>12</sup> Y236F bacterial SDH<sup>44</sup>). Despite this, the results from both computational approaches on simplified structural models clearly support the possibility of axial  $\text{Cl}^-$  coordination and the weakness of the ensuing Mo(V)-Cl interaction.

In order to investigate the proposed role of Arg in stabilizing the hypothesized axial  $\text{Cl}^-$  coordination, the above calculations were extended to include additional atoms of the SO active site, as shown in model A2 (Figure 9). Starting coordinates were prepared by placing  $\text{Cl}^-$  into each of the available *wt* SO crystal structures at the axial position, with the absolute minimum  $R_{\text{MoCl}}$  of 2.5 Å, and then determining the range of flexibility of the Arg residue within the modified protein environment. Because of the constraints imposed by the protein backbone itself, the Arg  $\alpha$  and  $\beta$  carbon positions were constrained and only movements beyond the  $\beta$  carbon were allowed. Furthermore, in order to minimize the number of artificial constraints required for geometry optimization, H-bonding interactions from the active site Tyr residue to the OH ligand and from the amide backbone to the oxo ligand were included, allowing the Cys and OH constraints to be removed.

Despite having the shortest possible  $R_{\text{MoCl}}$ , it was immediately clear in preparing model A2 that, as a consequence of the very limited amount of space available with  $\text{Cl}^-$  present, a

relatively high-energy conformation for Arg would be required in order to accommodate the  $\text{Cl}^-$  without considerable movement of either the protein backbone or the entire Mo cofactor. Nevertheless, with  $R_{\text{MoCl}}$  constrained, a plausible Arg position was identified where the Arg is folded under the  $\text{Cl}^-$ , toward the back of the positively charged channel, and forms a single H-bond to the  $\text{Cl}^-$ . During the geometry optimization, the presence of the  $\text{Cl}^-$  in the axial position resulted in the rotation of the OH ligand out of the equatorial plane to form a weak H-bonding interaction with the  $\text{Cl}^-$  (Figure 9), despite the additional interaction from the included Tyr residue with the OH ligand.

Property calculations on model A2 (Figure 9) revealed significant effects on the  $\text{Cl}^-$  and  $^{17}\text{O}$  ligand  $nqi$  and  $hfi$  parameters. The calculated isotropic  $\text{Cl}^-$   $hfi$  and  $nqi$  values of 10.2 MHz and 26.9 MHz, respectively, are both significantly larger than the experimental values and also than those of the analogous model at the same  $R_{\text{MoCl}}$  without Arg present (model A1, Figure 8 and Table 1). The calculated  $^{17}\text{O}$  oxo  $hfi$  and  $nqi$  are 6.51 MHz and 2.55 MHz, respectively, and are both similar to the experimental results. In the case of the  $^{17}\text{OH}$  oxygen, however, which is rotated out of the equatorial plane due to the axial  $\text{Cl}^-$ , the calculated  $hfi$  ( $a_{\text{iso}} = 0.72$  MHz) is not comparable to the experimental value since the  $^{17}\text{O}$  orbital overlap with the Mo-centered SOMO is disrupted, resulting in practically zero spin density on the  $^{17}\text{O}$  atom. In addition to these effects, the principal  $g$ -values calculated for this structure differ significantly from the experimental values (Table 1). The equatorial  $^{17}\text{OH}$   $nqi$ , however, is relatively unaffected by the orientation of the ligand, and its calculated value ( $e^2Qq/h = 8.02$  MHz) is practically identical to the previous axial  $\text{Cl}^-$  calculations for model A1.

When the geometry optimization is performed from the starting coordinates of model A2 and with the  $\text{Cl}^-$  geometric constraints removed, the Mo-Cl bond immediately breaks, and the  $\text{Cl}^-$  associates with the Arg, moving away from the axial coordination site to ultimately form a H-bond with the equatorial OH ligand. Except for the Arg, which chelates the  $\text{Cl}^-$  through two H-bonding interactions and is not H-bonded to the OH ligand, this geometry-optimized structure (model E1, Figure 10) is remarkably similar to that of the recombinant cSO (Mo-domain) crystal structure that contains  $\text{Cl}^-$  near the active site (PDB 2A99).<sup>32</sup>

The  $hfi$  and  $nqi$  results for the  $\text{Cl}^-$  of model E1 (Figure 10) are both in better agreement with the experimental values than any of the computational models having direct coordination of the  $\text{Cl}^-$  to the Mo (Table 1). Although the calculated  $\text{Cl}^-$  isotropic  $hfi$  of 1.49 MHz is still substantially lower than the experimental value, the calculated  $\text{Cl}^-$   $nqi$  value of 1.89 MHz is only slightly less than the experimental value of ~3 MHz. This trend is similar for the  $^{17}\text{O}$   $hfi$  parameters. The calculated oxo  $^{17}\text{O}$   $hfi$  ( $a_{\text{iso}} = 3.10$  MHz) and  $^{17}\text{OH}$  oxygen  $hfi$  ( $a_{\text{iso}} = 16.39$  MHz) in this case are both about half the experimental values, while the calculated  $nqi$  of the  $^{17}\text{O}$  oxo,  $e^2Qq/h = 0.97$  MHz, and the OH  $^{17}\text{O}$ ,  $e^2Qq/h = 6.64$  MHz, agree very well with their respective experimental values.

Another, more comprehensive alternative structural model for  $\text{Cl}^-$  binding was derived from the recent recombinant cSO (Mo-domain) crystal structure (PDB 2A99).<sup>32</sup> In that work, the enzyme was prepared with  $\text{SO}_4^{2-}$ -free buffer and in the presence of  $\text{Cl}^-$ . A single  $\text{Cl}^-$  was located at ~5 Å from the Mo center where it was directly H-bonded to the equatorial OH ligand ( $R_{\text{OCl}} = 2.31$  Å) and was also coordinated by two water molecules as well as residues R190 and W204.

Using the crystallographic coordinates from this structure, we prepared a computational model of the entire active site that, in addition to the amino acid residues and waters that directly interact with  $\text{Cl}^-$  and the OH ligand, includes amide H-bonding interactions from the protein backbone to each of these and to the Mo cofactor (model E2, Figure 11). This was done so that the geometry optimization could be performed with as few geometric constraints as possible,

thus improving the general quality and significance of the final property calculations. The geometry optimization was carried out with only water oxygen and protein backbone carbon atoms (or residue side chain carbon closest to the  $\alpha$  position where the backbone was not required) constrained to their relative Cartesian coordinate positions, leaving all other atoms fully relaxed. The geometry-optimized structure is shown in Figure 11.

Property calculations for model E2 (Figure 11) revealed generally better agreement with the experimental results (Table 1). Compared to all of the other computational models, the calculated  $\text{Cl}^-$   $hfi$  ( $a_{\text{iso}} = 1.86$  MHz) most closely agrees with the experimentally obtained value, although it remains low. The calculated  $\text{Cl}^-$   $nqi$  ( $e^2Qq/h = 2.10$  MHz), however, falls within the range of the experimentally obtained values. Similarly, the computed  $^{17}\text{O}$  oxo and  $^{17}\text{OH}$  ligand  $hfi$  results ( $a_{\text{iso}} = 3.44$  MHz and 8.67 MHz, respectively) were both underestimated compared with the experimentally obtained values, while excellent  $nqi$  agreement was obtained in both cases ( $e^2Qq/h = 1.00$  MHz and 6.50 MHz, respectively).

Table 1 summarizes all of the computed results for the systems with directly coordinated axial  $\text{Cl}^-$  (models A1 and A2) and for those with H-bonded  $\text{Cl}^-$  in the equatorial plane of the Mo active site (models E1 and E2). The calculations indicate clear differences in the spectroscopic parameters of the magnetic nuclei for the two types of structural possibilities, particularly for the  $^{35}\text{Cl}$  parameters. While the calculated  $hfi$  values are generally underestimated compared to the experimental values, it is important to emphasize that the  $hfi$  are extremely sensitive to the structure of the computational models and of the enzyme itself under the specific experimental conditions that the measurements were obtained. In this context, the computed  $hfi$  values are most reliable as a means of comparing one distinct system with another that has a significantly different electronic structure, such as between an inner-sphere equatorial vs. an inner-sphere axial Mo-Cl bonding interaction, where the Cl  $hfi$  differ by an order of magnitude or more. This sensitivity is also reflected in the differences in the principal  $g$ -values and in the high variance of the  $^{17}\text{O}$  and  $^1\text{H}$   $a_{\text{iso}}$  values for the  $^{17}\text{OH}$  ligand of the models, where slight differences in the  $\text{O}\equiv\text{Mo}-\text{O}-\text{H}$  dihedral angle (the OH rotation with respect to the metal x,y plane) within the same system result in very large differences between the ligand and metal orbital overlap, producing a large range of possible  $hfi$  values. While the  $hfi$  values calculated in this work for the  $^{35}\text{Cl}$ , oxo and hydroxo  $^{17}\text{O}$ , and the hydroxo  $^1\text{H}$  are all completely reasonable, they do not definitively distinguish between the structural possibilities of axial  $\text{Cl}^-$  coordination and H-bonded  $\text{Cl}^-$  in the equatorial plane of the Mo active site. The calculated  $g$ -values for the systems with H-bonded  $\text{Cl}^-$  in the equatorial plane (models E1 and E2), however, are in better agreement with the experimental values compared to the models with axially coordinated  $\text{Cl}^-$  (models A1 and A2).

In contrast to the high sensitivity of the  $hfi$  results to very small changes in the electronic structure of a system, the  $nqi$  results are sensitive to the electric field gradient created by the local environment (bonds and charges) near the quadrupolar nucleus. The axial inner-sphere coordination of  $\text{Cl}^-$  to the highly positive Mo(V) results in large  $^{35}\text{Cl}$   $nqi$  values that are many times greater than the experimental  $^{35}\text{Cl}$   $nqi$  results. The inclusion of the positively charged Arg residue to the axially coordinated  $\text{Cl}^-$  increases the  $nqi$  even further (Table 1). While the calculated  $nqi$  parameters for the  $^{35}\text{Cl}$  and the  $^{17}\text{O}$  oxo ligands of the axial models do not agree with the experimental values, excellent agreement is obtained for both of the systems with H-bonded  $\text{Cl}^-$  in the equatorial plane of the Mo active site, particularly for model E2, which was derived from the X-ray structure coordinates (PDB 2A99).

Finally, we return to the possibility of more than one nearby  $\text{Cl}^-$ , which was raised during the discussion of the simulation of the Cl ESEEM spectra. The above DFT calculations of the structures of SO active site models show that a neighboring  $\text{Cl}^-$  with an observed ESEEM and a measurable  $hfi$  can only be located in a general equatorial position, H-bonded to the OH

ligand. The flexibility of the protein environment in the substrate access channel is sufficient to accommodate a single neighboring  $\text{Cl}^-$ , but there seems to be insufficient space for two or more  $\text{Cl}^-$  ions, all of which would have to be H-bonded to the OH ligand. Therefore, the DFT structural analysis supports the assumption of a single neighboring  $\text{Cl}^-$  made in the simulations.

## CONCLUSIONS

ESEEM experiments on samples of *lpH* SO that were prepared with  $^{35}\text{Cl}$ - and  $^{37}\text{Cl}$ -enriched buffers, as well as with buffer containing the natural abundance of Cl isotopes, clearly demonstrate that  $\text{Cl}^-$  is located in close proximity to the Mo(V) center of *lpH* SO. When a *lpH* SO sample is prepared using buffer that contains only trace amounts of  $\text{Cl}^-$  (comparable to the SO concentration itself), the  $\text{Cl}^-$  signal remains unchanged with respect to the samples prepared with a large excess of  $\text{Cl}^-$ , indicating homogeneous binding of  $\text{Cl}^-$  to the Mo(V) active center. A survey of the ESEEM spectra from various preparations of sulfite oxidizing enzymes (different organisms, mutations, pH) has shown that the  $\text{Cl}^-$  signal in SO can only be detected in the *lpH* form and is not observed in the *hpH* or in the *blocked* forms of the enzymes. Interestingly, and in contrast to the suggestion elsewhere,<sup>14</sup> the presence of the  $\text{Cl}^-$  signal is not dependent on the interaction of Tyr (Y343 in hSO,<sup>12</sup> Y236 in bacterial SDH<sup>44</sup>) in the *lpH* SO active site.

In the absence of relevant structurally defined Mo(V) model systems, DFT calculations were used to evaluate two distinct types of structural models that describe the interaction of  $\text{Cl}^-$  with the SO active site; one type of model assumed the proposed direct axial coordination of the  $\text{Cl}^-$  to Mo, *trans* to the oxo ligand, and the other type assumed that the  $\text{Cl}^-$  was H-bonded to the equatorial OH ligand. A comparison of the calculated and experimental  $^{35}\text{Cl}$  *nqi* results strongly disfavors the proposed direct axial inner-sphere coordination of  $\text{Cl}^-$ . The possibility of  $\text{Cl}^-$  stabilization in that position through the interaction of the nearby Arg residue results in even poorer agreement. Moreover, the interaction of the Arg significantly weakens the Mo-Cl bond due to the steric and geometric constraints within the protein itself, and geometry optimization without constraints on the  $\text{Cl}^-$  position results in a structure in which the  $\text{Cl}^-$  is H-bonded to the equatorial OH ligand (model E1, Figure 10).

Of the structural possibilities for *lpH* SO investigated in this work, the best agreement between the experimental and calculated results is obtained for the computational model that is derived from the recent X-ray crystal structure of recombinant cSO (PDB 2A99),<sup>32</sup> in which a  $\text{Cl}^-$  is H-bonded to the equatorial OH ligand in the equatorial plane of the Mo center (Model E2, Figure 11). In this case, the calculated *nqi* values for the  $^{35}\text{Cl}$  and  $^{17}\text{O}$  atoms each correspond to the range of experimental values. The *hfi* values are comparable to the results from the axial models, but remain lower than the experimental values. These discrepancies may reflect slight differences between the electronic structures and the resulting spin densities of the computational models and the known distribution of structures for *lpH* SO under the conditions required for the EPR studies (low pH, 20 K).<sup>11, 15, 48</sup>

Truncation of the active site models and imposed structural constraints strongly affect the calculated spectroscopic parameters. Additionally, any inherent limitations in the current computational methods will also contribute to the differences between the calculated and experimental values in Table 1. Nonetheless, this study clearly demonstrates that combining theoretical calculations with high resolution experimental measurements of the *hfi* and *nqi* parameters for magnetic nuclei and the principal *g*-values can provide significant insight concerning the structure of the Mo(V) active site of SO. Finally, although the structural and/or catalytic role of  $\text{Cl}^-$  (if any) in the active site of SO remains unclear, this work provides an immediate foundation for reevaluating the spectroscopic properties of *lpH* SO with other

halides ( $F^-$ ,  $Br^-$ , and  $I^-$ )<sup>4, 14</sup> and for investigating the active site Mo(V) structures of other molybdenum enzymes and their catalytically compromised mutants.

## Supplementary Material

Refer to Web version on PubMed Central for supplementary material.

## Acknowledgments

We gratefully acknowledge support of this research by the NIH (GM-37773 to JHE) and by grants from the NSF (DBI-0139459, DBI-9604939, BIR-9224431) and the NIH (S10RR020959) for development of the pulsed EPR facility. FN gratefully acknowledges financial support of this work by the German Science Foundation (grant NE 690/6-1). We thank Prof. K. V. Rajagopalan and Dr. H. L. Wilson for providing a sample of hSO. Samples of SDH proteins were from previous collaborations with Dr. Ulrike Kappler,<sup>44</sup> and samples of At-SO were from a previous investigation with Prof. Russ Hille.<sup>10</sup> We thank Dr. Arnold Raitsimring for helpful discussions.

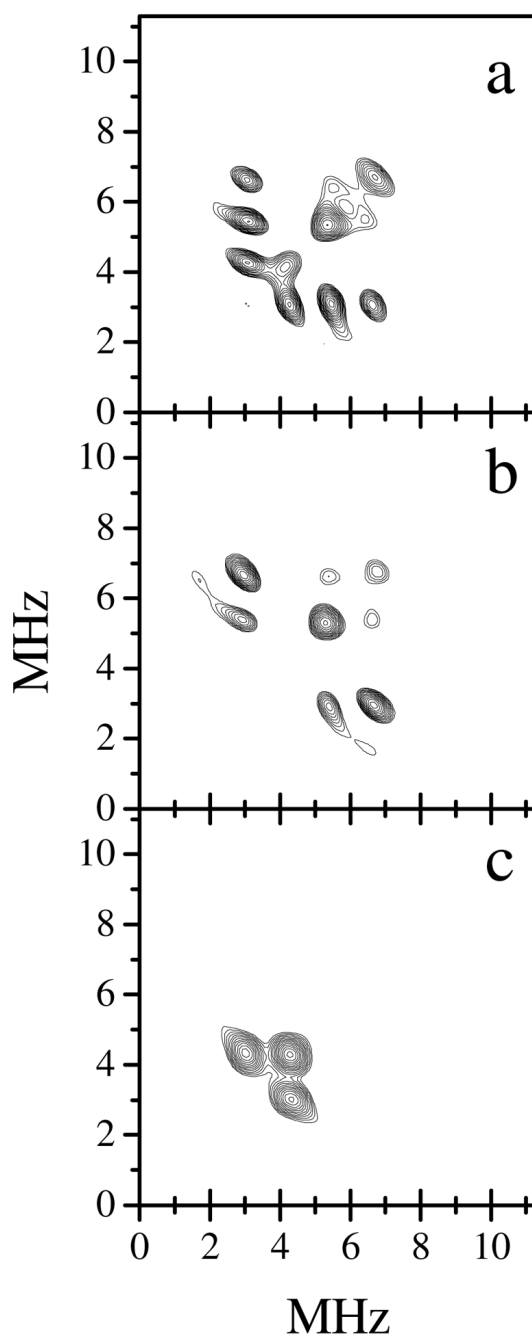
## References

1. (a) Kappler U, Bailey S. J Biol Chem 2005;280:24999. [PubMed: 15863498] (b) Schrader N, Fischer K, Theis K, Mendel RR, Schwarz G, Kisker C. Struct 2003;11:1251.
2. Kisker C, Schindelin H, Pacheco A, Wehbi WA, Garrett RM, Rajagopalan KV, Enemark JH, Rees DC. Cell 1997;91:973. [PubMed: 9428520]
3. Hille R. Chem Rev 1996;96:2757. [PubMed: 11848841]
4. Bray RC, Gutteridge S, Lamy MT, Wilkinson T. Biochem J 1983;211:227. [PubMed: 6307274]
5. (a) Cohen HJIF, Rajagopalan KV. J Biol Chem 1971;246:374. [PubMed: 5100417] (b) George GN, Garrett RM, Graf T, Prince RC, Rajagopalan KV. J Am Chem Soc 1998;120:4522. (c) Gutteridge S, Lamy MT, Bray RC. Biochem J 1980;191:285. [PubMed: 6258584] (d) Kessler DL, Rajagopalan KV. J Biol Chem 1972;247:6566. [PubMed: 4342603]
6. Lamy MT, Gutteridge S, Bray RC. Biochem J 1980;185:397. [PubMed: 6249254]
7. Rajagopalan, KV. Molybdenum and Molybdenum-Containing Enzymes. Vol. 1. Coughlan, MP., editor. Pergamon Press: Oxford; New York; 1980. p. 241
8. Eilers T, Schwarz G, Brinkmann H, Witt C, Richter T, Nieder J, Koch B, Hille R, Hänsch R, Mendel RR. J Biol Chem 2001;276:46989. [PubMed: 11598126]
9. Kappler U, Bennett B, Rethmeier J, Schwarz G, Deutzmann R, McEwan AG, Dahl C. J Biol Chem 2000;275:13202. [PubMed: 10788424]
10. Astashkin AV, Johnson-Winters K, Klein EL, Byrne RS, Hille R, Raitsimring AM, Enemark JH. J Am Chem Soc 2007;129:14800. [PubMed: 17983221]
11. Astashkin AV, Johnson-Winters K, Klein EL, Feng C, Wilson HL, Rajagopalan KV, Raitsimring AM, Enemark JH. J Am Chem Soc 2008;130:8471. [PubMed: 18529001]
12. Raitsimring AM, Astashkin AV, Feng C, Wilson HL, Rajagopalan KV, Enemark JH. Inorg Chim Acta 2008;361:941.
13. George GN, Kipke CA, Prince RC, Sunde RA, Enemark JH, Cramer SP. Biochemistry 1989;28:5075. [PubMed: 2548601]
14. Doonan CJ, Wilson HL, Bennett B, Prince RC, Rajagopalan KV, George GN. Inorg Chem 2008;47:2033. [PubMed: 18271529]
15. Astashkin AV, Hood BL, Feng CJ, Hille R, Mendel RR, Raitsimring AM, Enemark JH. Biochemistry 2005;44:13274. [PubMed: 16201753]
16. Raitsimring AM, Pacheco A, Enemark JH. J Am Chem Soc 1998;120:11263.
17. Raitsimring AM, Astashkin AV, Feng CJ, Enemark JH, Nelson KJ, Rajagopalan KV. J Biol Inorg Chem 2003;8:95. [PubMed: 12459903]
18. Astashkin AV, Klein EL, Enemark JH. J Inorg Biochem 2007;101:1623. [PubMed: 17644181]
19. Pacheco A, Basu P, Borbat P, Raitsimring AM, Enemark JH. Inorg Chem 1996;35:7001. [PubMed: 11666879]



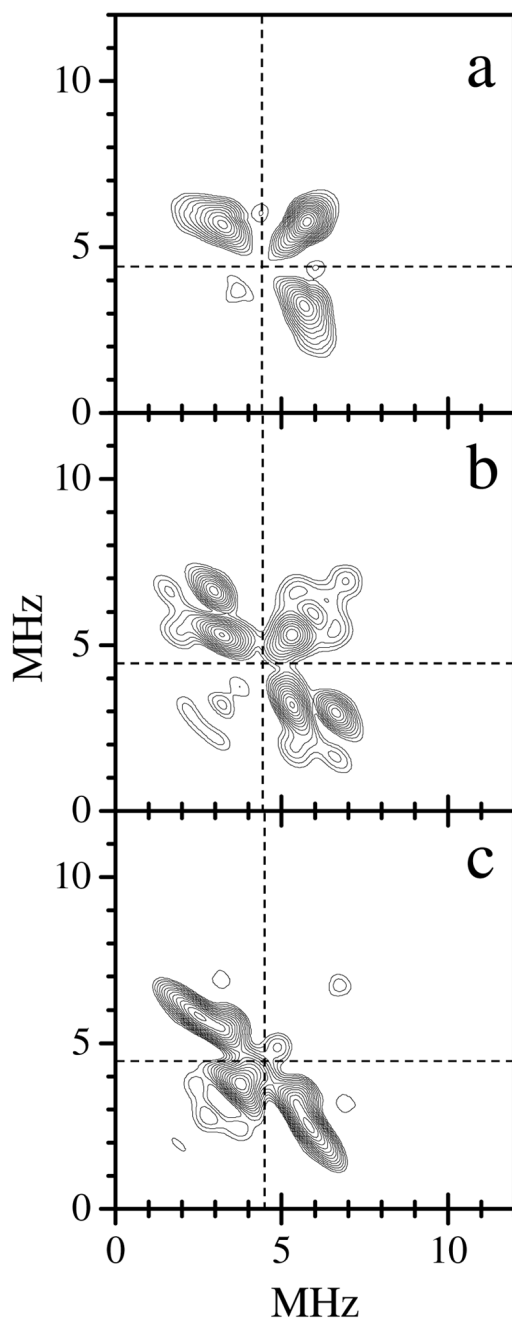
20. Astashkin AV, Enemark JH, Raitsimring AM. Concepts Magn Reson Part B (Magn Reson Engineering) 2006;29B:125.
21. <http://quiz2.chem.arizona.edu/epr>.
22. <http://www.thch.uni-bonn.de/tc/orca/>.
23. (a) Becke AD. Phys Rev A 1988;38:3098. [PubMed: 9900728] (b) Perdew JP. Phys Rev B 1986;33:8822.
24. (a) Schäfer A, Horn H, Ahlrichs R. J Chem Phys 1992;97:2571. (b) Schäfer A, Huber C, Ahlrichs R. J Chem Phys 1994;100:5829. Weigend, F.; Haeser, M.; Patzelt, H.; Ahlrichs, R. 2006. <ftp://ftp.chemie-karlsruhe.de/pub/basen>
25. Pantazis DA, Chen XY, Landis CR, Neese F. J Chem Theory Comput 2008;4:908.
26. Klamt A, Schüürmann G. J Chem Soc, Perkin Trans 1993;2:799.
27. Sinnecker S, Neese F. J Comput Chem 2006;27:1463. [PubMed: 16807973]
28. (a) Baerends EJ, Ellis DE, Ros P. Chem Phys 1973;2:41. (b) Dunlap BI, Connolly JWD, Sabin JR. J Chem Phys 1979;71:3396. (c) Eichkorn K, Treutler O, Öhm H, Häser M, Ahlrichs R. Chem Phys Lett 1995;240:283. (d) Eichkorn K, Weigend F, Treutler O, Ahlrichs R. Theor Chem Acc 1997;97:119.
29. van Lenthe E, Baerends EJ, Snijders JG. J Chem Phys 1993;99:4597.
30. van Wüllen C. J Chem Phys 1998;109:392.
31. van Lenthe JH, Faas S, Snijders JG. Chem Phys Lett 2000;328:107.
32. Karakas E, Wilson HL, Graf TN, Xiang S, Jaramillo-Busquets S, Rajagopalan KV, Kisker C. J Biol Chem 2005;280:33506. [PubMed: 16048997]
33. Doonan CJ, Wilson HL, Rajagopalan KV, Garrett RM, Bennett B, Prince RC, George GN. J Am Chem Soc 2007;129:9421. [PubMed: 17608478]
34. (a) Becke AD. J Chem Phys 1993;98:5648. (b) Lee C, Yang W, Parr RP. Phys Rev B 1988;37:785.
35. van Lenthe E, Baerends EJ. J Chem Phys 2000;112:8279.
36. Neese F, Wolf A, Fleig T, Reiher M, Hess BA. J Chem Phys 2005;122:204107/1. [PubMed: 15945713]
37. van Lenthe E, van der Avoird A, Wormer PES. J Chem Phys 1998;108:4783.
38. Höfer P, Grupp A, Nebenführ H, Mehring M. Chem Phys Lett 1986;132:279.
39. Matar K, Goldfarb D. J Chem Phys 1992;96:6464.
40. Astashkin AV, Neese F, Raitsimring AM, Cooney JJA, Bultman E, Enemark JH. J Am Chem Soc 2005;127:16713. [PubMed: 16305262]
41. van Doorslaer S, Schweiger A. Chem Phys Lett 1997;281:297.
42. Astashkin AV, Raitsimring AM. J Magn Reson 2000;143:280. [PubMed: 10729254]
43. The buffer [Cl] of ~ 1 mM was estimated from the manufacturer specifications for the individual buffer contents.
44. Kappler U, Bailey S, Feng CJ, Honeychurch MJ, Hanson GR, Bernhardt PV, Tollin G, Enemark JH. Biochemistry 2006;45:9696. [PubMed: 16893171]
45. manuscript in preparation.
46. Semin, GK.; Babushkina, TA.; Jakobson, GG. Nuclear Quadrupole Resonance in Chemistry. John Wiley & Sons; New York: 1975.
47. Astashkin AV, Feng C, Raitsimring AM, Enemark JH. J Am Chem Soc 2005;127:502. [PubMed: 15643856]
48. Enemark JH, Astashkin AV, Raitsimring AM. Dalton Trans 2006:3501. [PubMed: 16855750]
49. Calibration calculations for the Cl *hfi* and *nqi* were carried out on small molecules for which these parameters had been experimentally determined. In each case, the computational results were consistently accurate when compared with the experimentally determined values. Consequently, the discrepancies between the calculated and experimental values here are most likely due to the inherent imperfections of the computational models rather than the methodology itself.





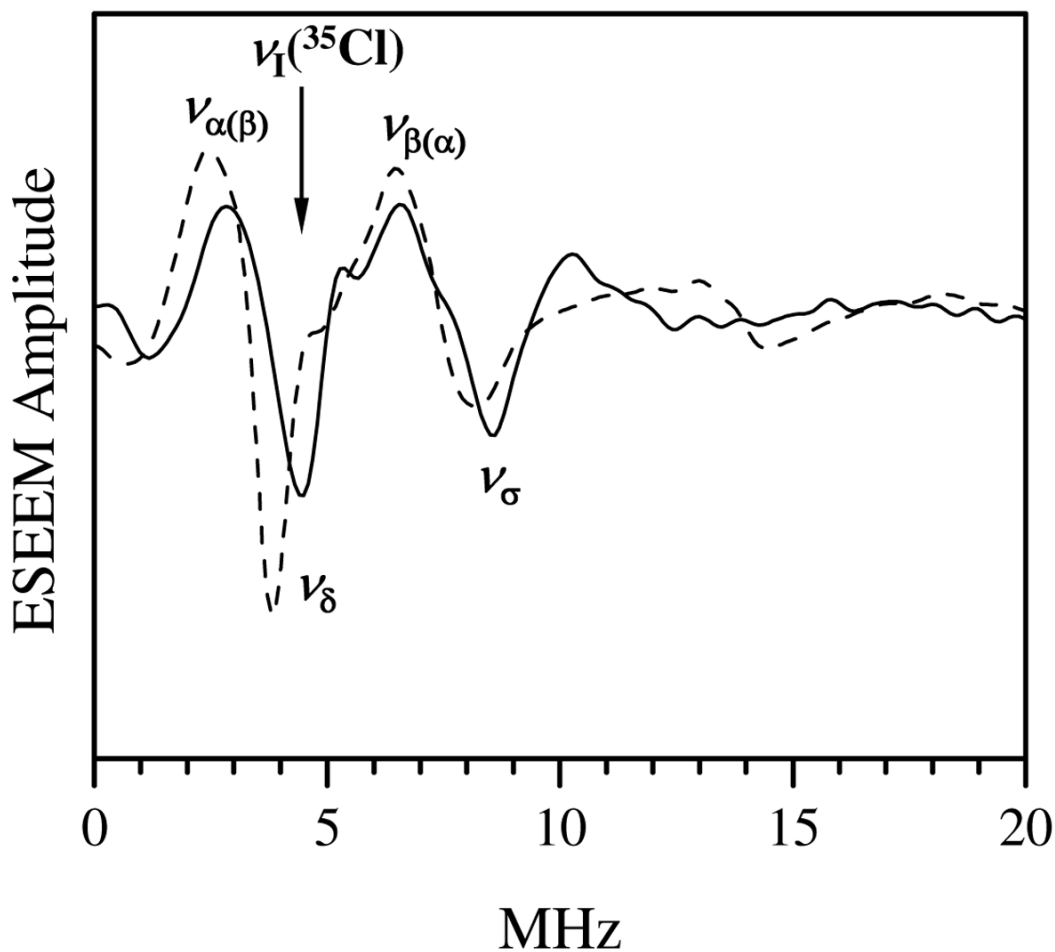
**Figure 1.**

Panels a, b and c, (+,+) quadrants of HYSCORE spectra of *l* pH Cl-SO, <sup>35</sup>Cl-SO and <sup>37</sup>Cl-SO, respectively. Experimental conditions:  $\nu_{\text{mw}} = 29.562$  GHz;  $B_0 = 1075.6$  mT ( $g_y$ ); time interval between the first and second mw pulses,  $\tau = 200$  ns; mw pulses, 15, 15, 27, 15 ns; temperature, 21 K.



**Figure 2.**

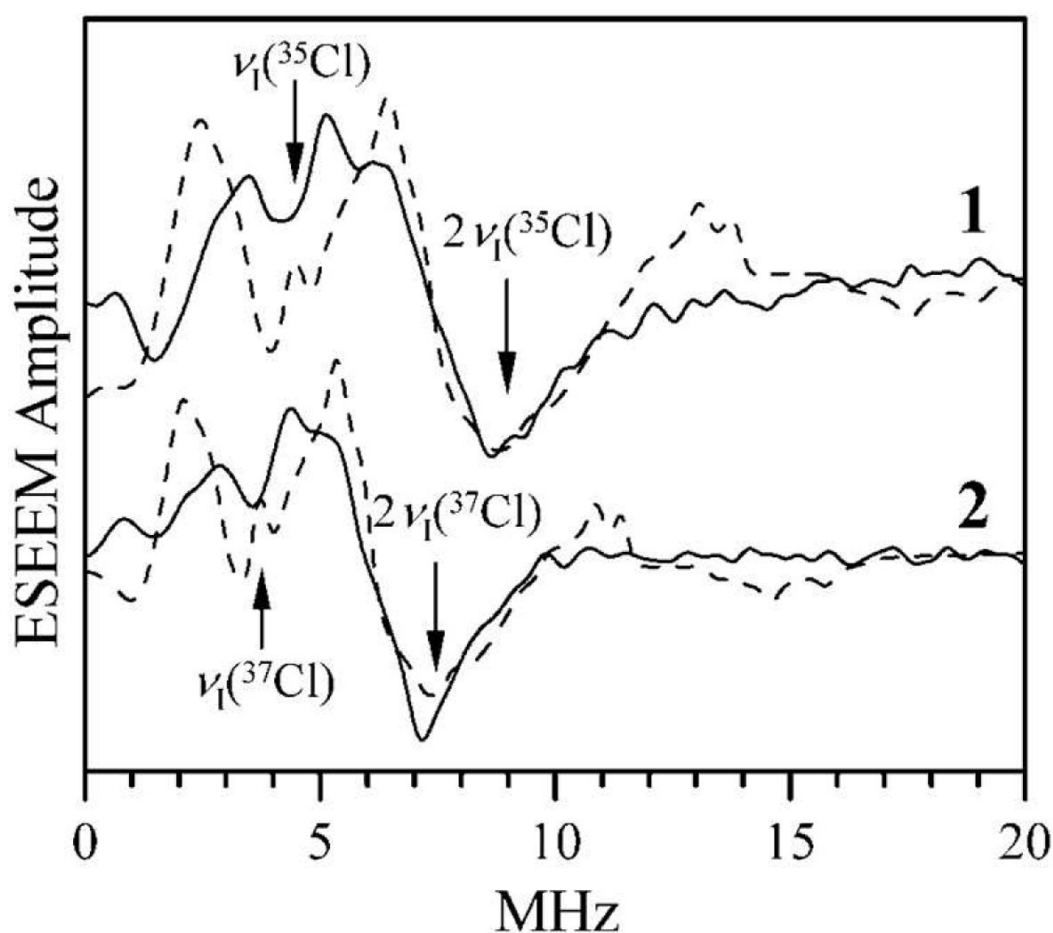
Panels a, b and c, (++) quadrants of HSCORE spectra of *l*-pH  $^{35}\text{Cl}$ -SO obtained at  $B_0 = 1059.7$  mT ( $g_z$ ), 1075.6 mT ( $g_y$ ) and 1078 mT ( $g_x$ ), respectively. Each spectrum represents a sum of the spectra obtained at  $\tau = 170, 200$  and 240 ns. Other experimental conditions:  $\nu_{\text{mw}} = 29.562$  GHz; mw pulses, 15, 15, 27, 15 ns; temperature, 21 K. Dashed lines show the Zeeman frequency of  $^{35}\text{Cl}$ .



**Figure 3.**

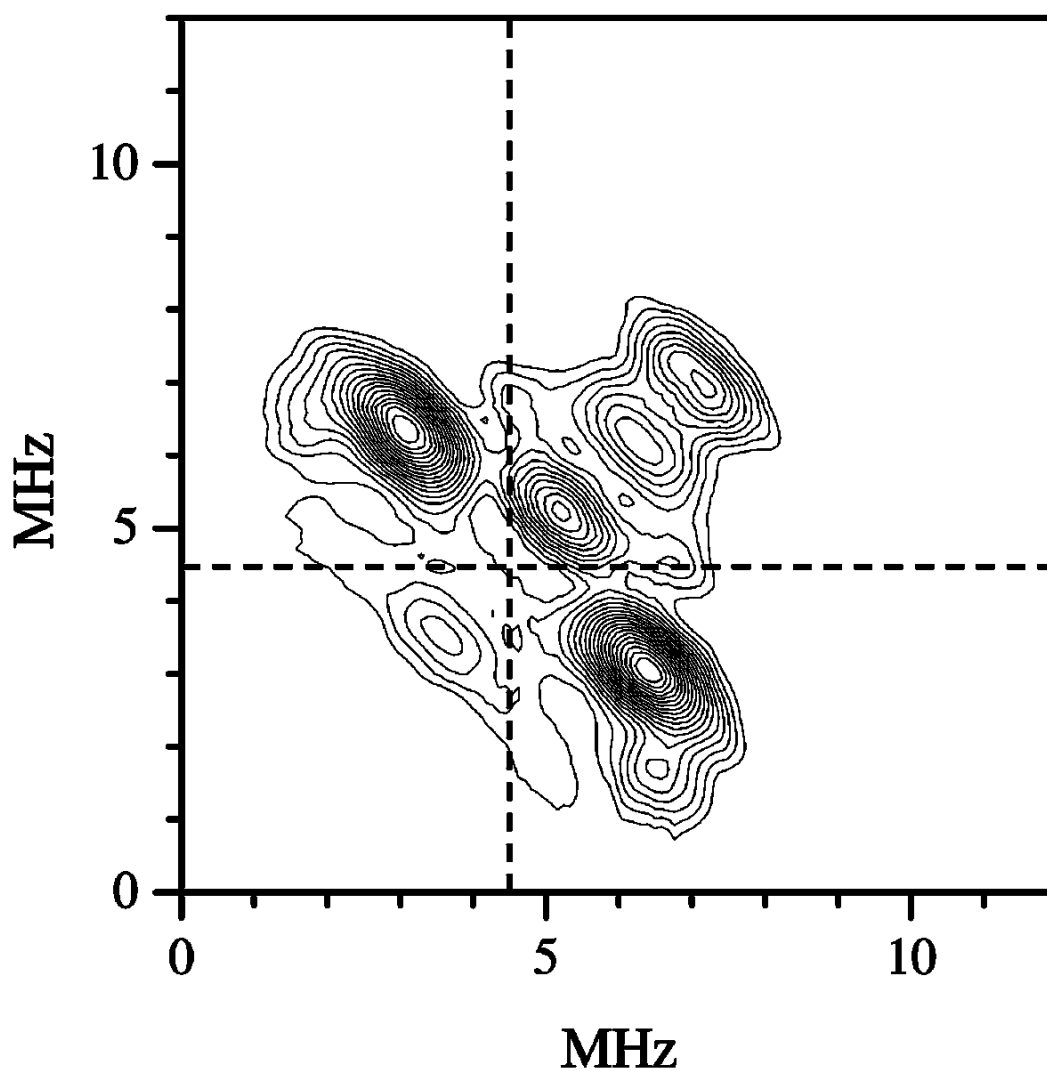
Solid trace, field-integrated two-pulse ESEEM spectrum (cosine FT) of  $lpH$   $^{35}\text{Cl-SO}$ .

Experimental conditions:  $\nu_{\text{mw}} = 29.562$  GHz; mw pulses,  $2 \times 15$  ns; temperature, 21 K. Dashed line, simulation for a  $^{35}\text{Cl}$  nucleus with  $a_{\text{iso}} = 4$  MHz,  $T_{\perp} = -0.2$  MHz,  $e^2Qq/h = 3$  MHz,  $\eta = 0.5$ . The orientation of the  $hfi$  tensor axis with respect to the  $nqi$  frame is given by  $\theta = 90^\circ$ ,  $\phi = 0^\circ$ ,  $\psi = 0^\circ$ .



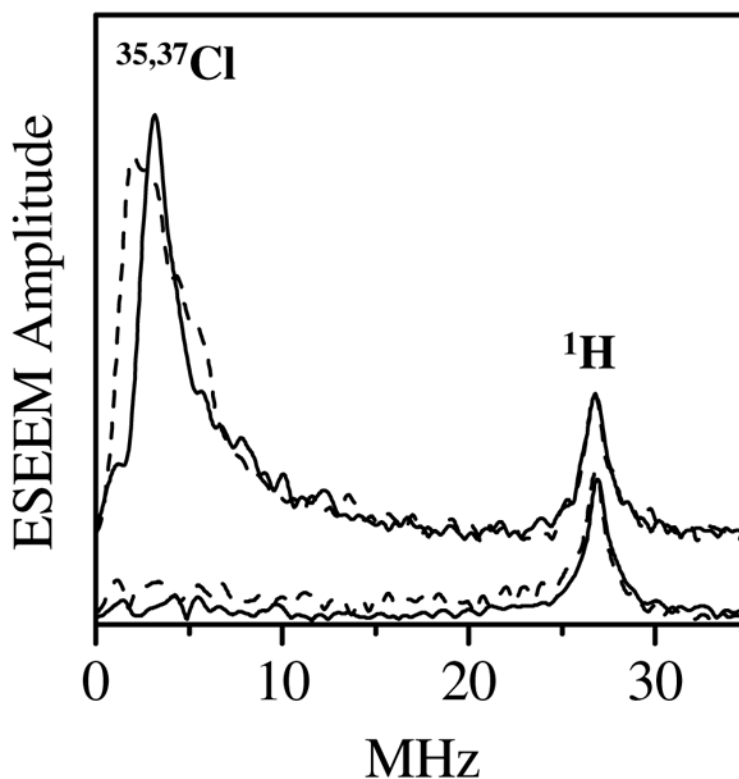
**Figure 4.**

Solid traces 1 and 2, field-integrated spectra (cosine FT) of  $\tau$ -integrated four-pulse ESEEM of  $^{35}\text{Cl-SO}$  and  $^{37}\text{Cl-SO}$ , respectively. Experimental conditions:  $\nu_{\text{mw}} = 29.562$  GHz; mw pulses, 15, 15, 27, 15 ns; temperature, 21 K. Dashed trace 1, simulation for  $^{35}\text{Cl}$  with parameters given in Figure 1 caption. Dashed trace 2, simulation for  $^{37}\text{Cl}$  with parameters obtained from those of  $^{35}\text{Cl}$  by scaling according to the ratios of magnetic and quadrupole moments:  $a_{\text{iso}} = 3.3$  MHz,  $T_{\perp} = -0.17$  MHz,  $e^2Qq/h = 2.4$  MHz,  $\eta = 0.5$ .



**Figure 5.**

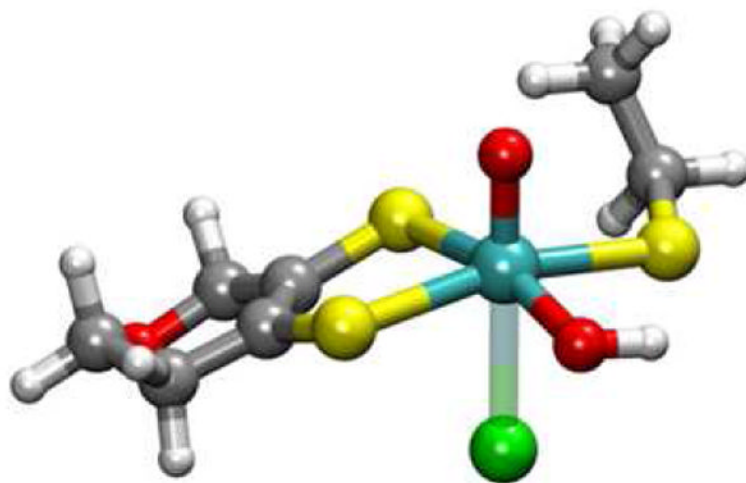
(++) quadrant of HYSCORE spectrum of *lpH* hSO prepared with the buffer containing no chloride. Experimental conditions:  $\nu_{\text{mw}} = 29.600$  GHz;  $B_0 = 1077$  mT ( $g_y$ ); time interval between the first and second mw pulses,  $\tau = 200$  ns; mw pulses, 15, 15, 28, 15 ns; temperature, 21 K. Dashed lines show the Zeeman frequency of the main chlorine isotope,  $^{35}\text{Cl}$  (75.76% natural abundance).



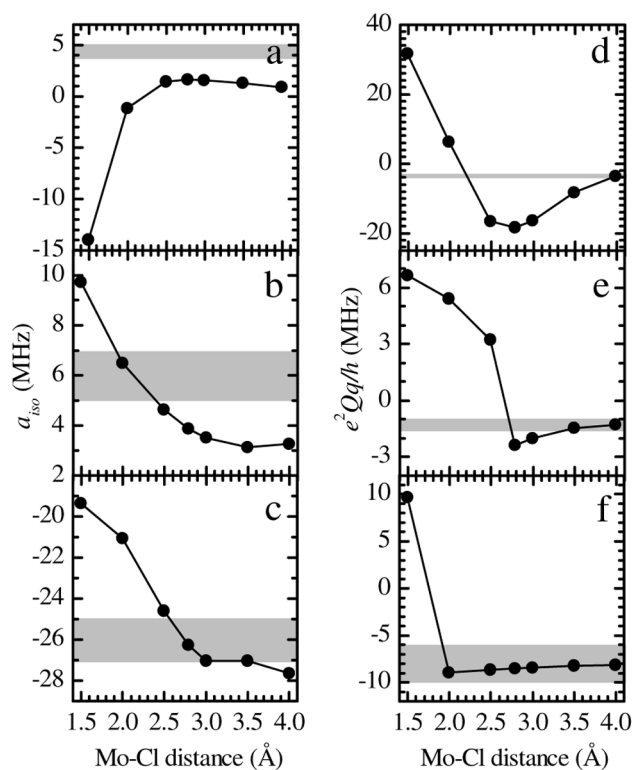
**Figure 6.**

$K_u$ -band primary ESEEM spectra (amplitude FT) of different samples of SO or SDH obtained at  $g_Y$ . Top solid trace, *lpH* cSO; top dashed trace, *lpH* Y236F SDH; bottom solid trace, *hpH* cSO; bottom dashed trace, *blocked* form of At-SO. Experimental conditions for the *lpH* cSO, *lpH* Y236F SDH, *hpH* cSO and *blocked* At-SO:  $\nu_{mw} = 17.341$  GHz, 17.274 GHz, 17.270 GHz, and 17.368 GHz, respectively;  $B_0 = 630.8$  mT, 625.1 mT, 630.7 mT, and 631.5 mT – At), respectively; mw pulses,  $2 \times 15$  ns; temperature, 21 K.





**Figure 7.** Representative structure (model A1, where  $R_{\text{MoCl}} = 2.80 \text{ \AA}$ ) of the minimum computational models for constrained axial  $\text{Cl}^-$  binding to the Mo(V) center of *lpH* SO.

**Figure 8.**

The  $hfi$  (a, b, c) and  $nqi$  (d, e, f) parameters of  $^{35}\text{Cl}$  (a, d), oxo- $^{17}\text{O}$  (b, e), and the  $^{17}\text{O}$  from the equatorial OH ligand (c, f) calculated by DFT as a function of  $R_{\text{MoCl}}$  for model A1 (Figure 7). The ranges of experimental parameters are shown for reference as horizontal strips.

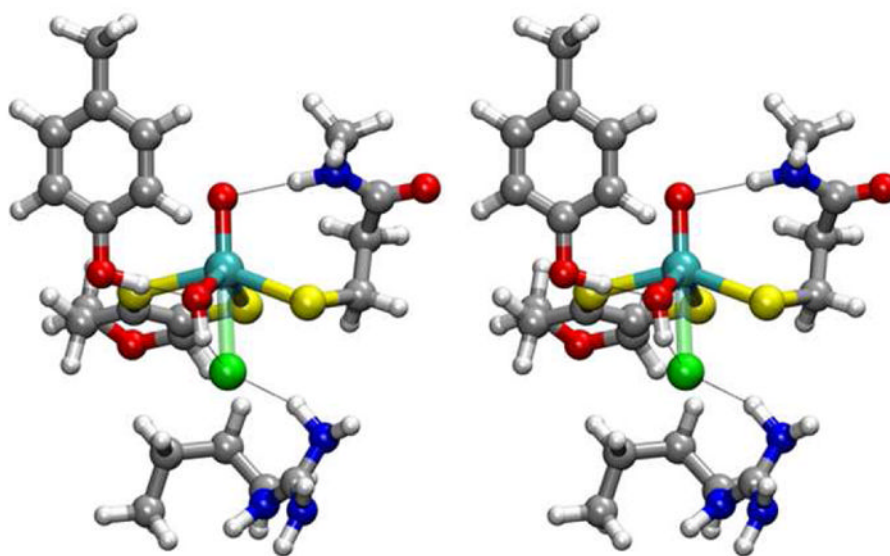


**Figure 9.**

Stereo view (cross-eye) of the geometry-optimized computational model A2, where  $R_{\text{MoCl}}$  is constrained to 2.50 Å and the proposed Arg interaction with the axially bound  $\text{Cl}^-$  is included.

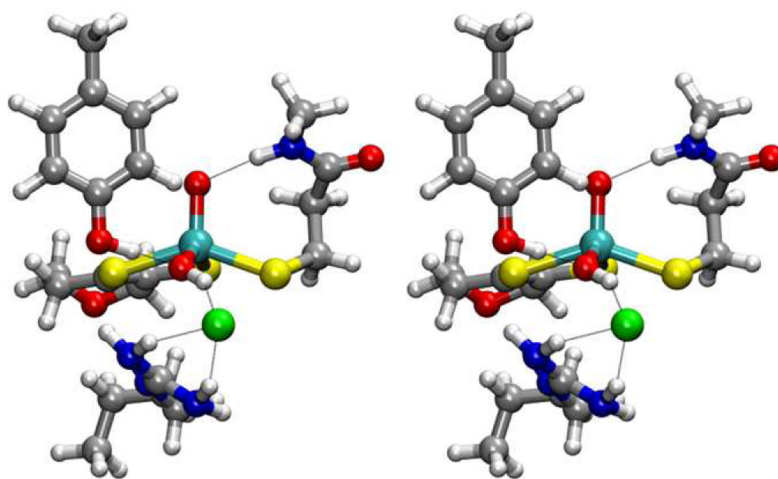


**Figure 10.** Stereo view (cross-eye) of the computational model E1 that is obtained from model A2 (Figure 9) when geometry optimization is performed without Cl geometric constraints.

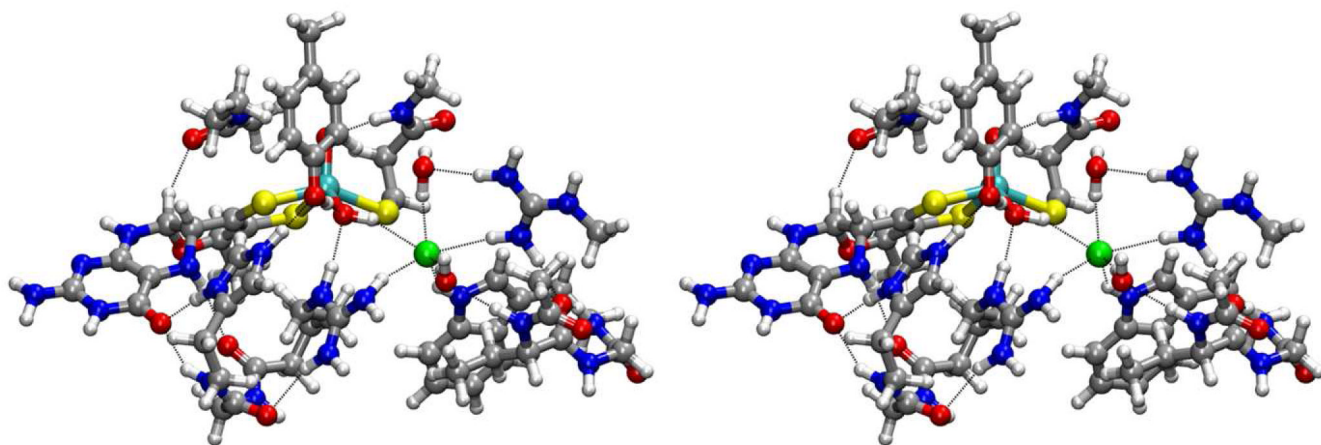


**Figure 11.** Stereo view (cross-eye) of the geometry-optimized computational model E2 that was obtained from geometry optimization of the X-ray crystal coordinates from recombinant cSO with Cl<sup>-</sup> near the Mo center (PDB 2A99).

**Table 1**  
Theoretical and Experimental Parameters for the Computational Models and *IpH* SO.

system	$g_x$	$g_y$	$g_z$	$^{35}\text{Cl}$			oxo- $^{17}\text{O}$			hydroxo- $^{17}\text{O}$			hydroxo- $^1\text{H}$ $a_{\text{iso}}$ (MHz)
				$a_{\text{iso}}$ (MHz)	$e^2Qq/h$ (MHz)		$a_{\text{iso}}$ (MHz)	$e^2Qq/h$ (MHz)		$a_{\text{iso}}$ (MHz)	$e^2Qq/h$ (MHz)		
model A1, Figure 7 ( $R_{\text{MoCl}} = 2.80$ $\text{\AA}$ )	1.947	1.969	2.000	1.52	18.70		3.84	2.39		26.27	8.48		47.86
model A2, Figure 9 ( $R_{\text{MoCl}} = 2.50$ $\text{\AA}$ )	2.002	2.018	2.019	10.19	26.90		6.52	2.55		0.72	8.02		0.50
model E1, Figure 10	1.964	1.973	2.004	1.49	1.89		3.10	0.97		16.39	6.64		38.81
model E2, Figure 11 (from PDB 2A99)	1.971	1.977	2.017	1.86	2.10		3.44	1.00		8.67	6.50		24.53
<i>IpH</i> SO (experimental values)	1.967	1.972	2.004	4.5(5)	3(1)		6(1)	1.5(5)		26(1)	8(2) <sup>a</sup>		26(1)

<sup>a</sup>The quadrupole coupling constant,  $e^2Qq/h$ , for the hydroxo- $^{17}\text{O}$  has not yet been evaluated specifically for Mo(V) complexes. This value is the expected value based on the known  $^{17}\text{O}$  quadrupole coupling constant of  $^{17}\text{O}$ -labeled water and hydroxide.